Interfacial Strain Engineering Induces Fatigue-Resistant, High-Capacity Photo-Assisted Lithium Storage

Mudasar Nazir[1], Kiem G. Nguyen[1], Richard T. Baker[2], Matthew E Berry[3], Rabia Khatoon[1], Shumaila Babar[1], Steven Dunn[1], Suela Kellici[1], and Muhammad Tariq Sajjad[1]**

[1]School of Engineering and Design, London South Bank University, 103 Borough Road, London, SE1 0AA UK

[2]EaStChem School of Chemistry, University of St Andrews, St Andrews KY16 9ST, UK

[3]Edinburgh Instruments Ltd., Livingston EH54 7DQ, UK

Email: kellicis@lsbu.ac.uk (SK); sajjadt@lsbu.ac.uk (M.T.S)

1. Structural Characterisation

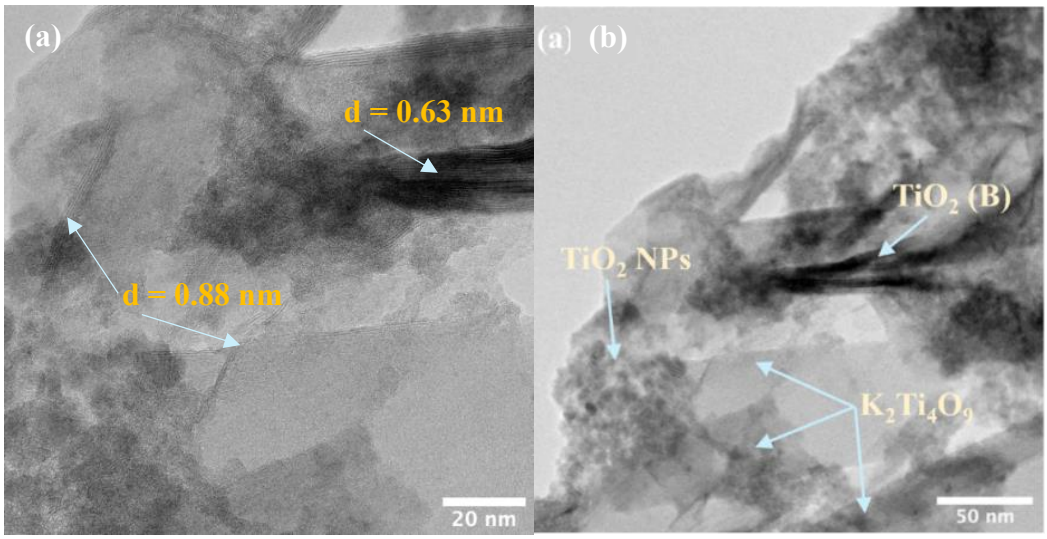

Figure S1: ***High-resolution TEM analysis of the $TiO_2/K_2Ti_4O_9$–rGO nanocomposite. (a)*** *Lattice-resolved HR-TEM image showing an interplanar spacing of ~0.88 nm (layered $K_2Ti_4O_9$) and ~0.63 nm (TiO_2(B)). (**b**) High-resolution TEM images showing coexisting anatase TiO_2 nanoparticles, TiO_2(B) nanorods, and $K_2Ti_4O_9$ platelets anchored on rGO, forming an integrated multiphase framework. Lattice bending and fringe distortion at phase boundaries are consistent with local lattice distortion and elastic strain.*

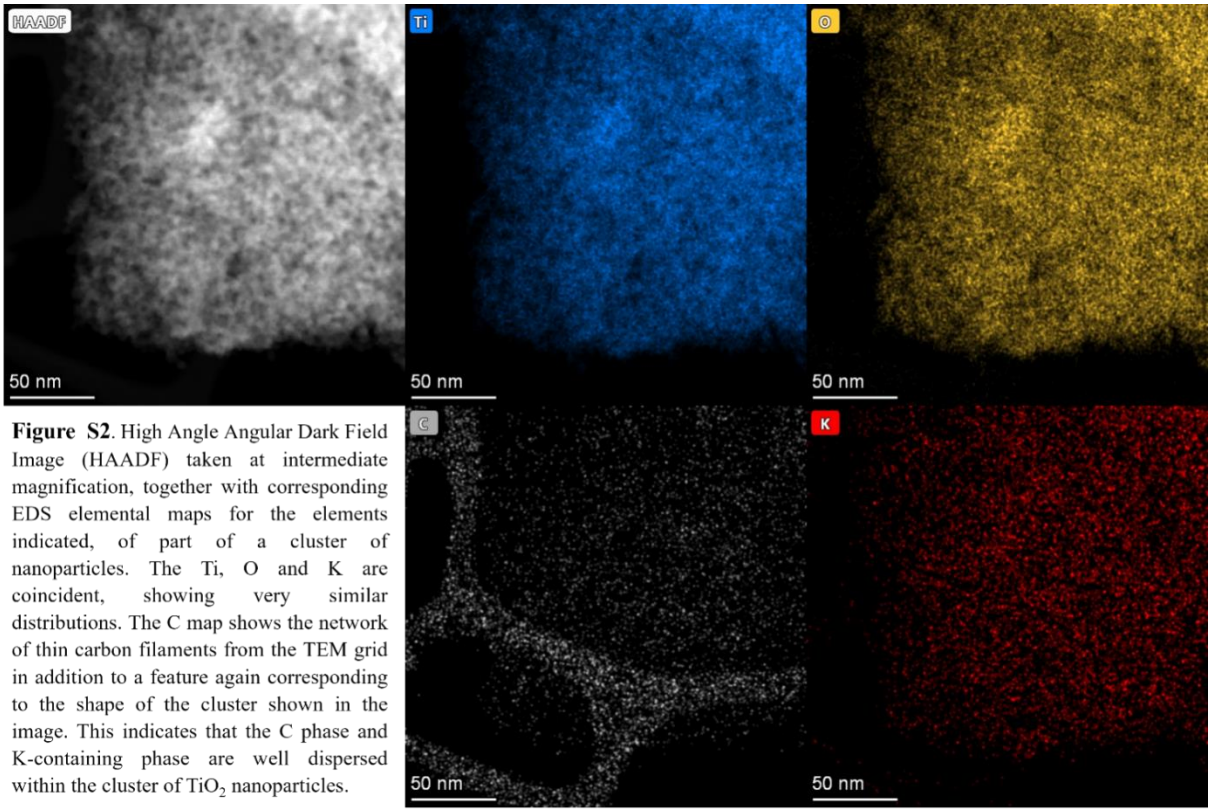

Figure S2. High Angle Angular Dark Field Image (HAADF) taken at intermediate magnification, together with corresponding EDS elemental maps for the elements indicated, of part of a cluster of nanoparticles. The Ti, O and K are coincident, showing very similar distributions. The C map shows the network of thin carbon filaments from the TEM grid in addition to a feature again corresponding to the shape of the cluster shown in the image. This indicates that the C phase and K-containing phase are well dispersed within the cluster of TiO_2 nanoparticles.

2. Surface Chemistry and Elemental Composition

X-ray photoelectron spectroscopy (XPS) was used to examine the surface composition and chemical states of the $TiO_2/K_2Ti_4O_9$–rGO nanocomposite (**Figure S3**). All binding energies were charge-corrected using the C 1s reference at 284.8 eV. Core-level spectra confirm the presence of Ti, K, O, and C without detectable impurity phases. For the high-resolution spectra, Ti 2p was interpreted using Ti^{4+} and lower-binding-energy Ti^{3+} contributions, while O 1s was resolved into lattice oxygen, defect/hydroxyl-related oxygen, and higher-binding-energy adsorbate components. Quantitative analysis of survey spectra (**Table S1**) reveals elemental ratios consistent with the designed multiphase architecture.

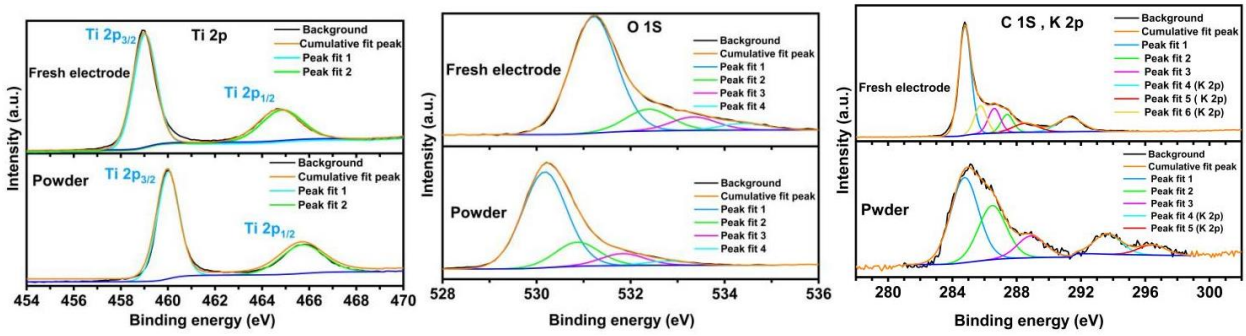

Figure S3: ***High-resolution XPS spectra of the synthesised $TiO_2/K_2Ti_4O_9$–rGO nanocomposite.*** *Core-level spectra confirm the presence and chemical states of Ti, K, O, and C, verifying successful formation of the multiphase oxide–carbon composite without detectable impurity phases.*

Table S1: ***Elemental Composition (atomic %) of $TiO_2/K_2Ti_4O_9$-rGO by XPS.*** *Values represent average atomic percentages derived from survey spectra.*

Elemental compositions (%)			
C	**K**	**Ti**	**O**
34.4	8.7	15.0	41.9

3. Strain Estimation by Raman Spectroscopy

Interfacial strain within the $TiO_2/K_2Ti_4O_9$–rGO nanocomposite was evaluated using Raman spectroscopy. The relationship between Raman peak shift (Δω) and strain (ε) is given by[1,2]:

$$\varepsilon = -\frac{\Delta\omega}{\gamma.\,\omega_o} \tag{1}$$

where ω_0 is the unstrained Raman mode frequency and γ is the Grüneisen parameter.
Considering the interatomic bonding characteristics of TiO_2, the sum of attractive and repulsive potential exponents (a + r = 3) was adopted.

$$\omega = \omega_o\left(1 - \frac{a+r+3}{2}\varepsilon\right) \tag{2}$$

This approach enables quantitative estimation of strain induced by multiphase coupling and lattice mismatch at the oxide–oxide and oxide–carbon interfaces.

$$\omega = \omega_o(1 - 3\varepsilon) \tag{3}$$

Using the shift from 146.6 to 153.1 cm^{-1} yields an approximate effective compressive strain of ~1.5%. This value is derived from the shift of the anatase E_g Raman mode; however, phonon confinement, finite crystallite size, surface stress, and local disorder may also influence the E_g position and linewidth in nanocrystalline TiO_2. Together with the HRTEM observations of lattice bending and fringe distortion, this therefore represents the best approximate strain estimate for the multiphase composite.

4. Optical Properties and Bandgap Determination

Diffuse reflectance UV–Vis spectroscopy was used to investigate the optical properties of the $TiO_2/K_2Ti_4O_9$–rGO nanocomposite. The Kubelka–Munk transformation, $F(R)$, was applied to convert reflectance data into absorbance-like spectra, and Tauc-type plots were used to estimate optical gaps.

$$\mathrm{F(R)} = \frac{K}{S} = \frac{(1-R)^2}{2R} \tag{4}$$

Plots of $(F(R)h\nu)^{1/a}$ versus photon energy (hν) were used to estimate direct (a = 0.5) and indirect (a = 2) optical bandgaps (**Figure S4**). The multiphase $TiO_2/K_2Ti_4O_9$–rGO composite exhibits broadened optical absorption relative to single-phase TiO_2, reflecting synergistic electronic interactions among TiO_2 polymorphs, $K_2Ti_4O_9$, and rGO.

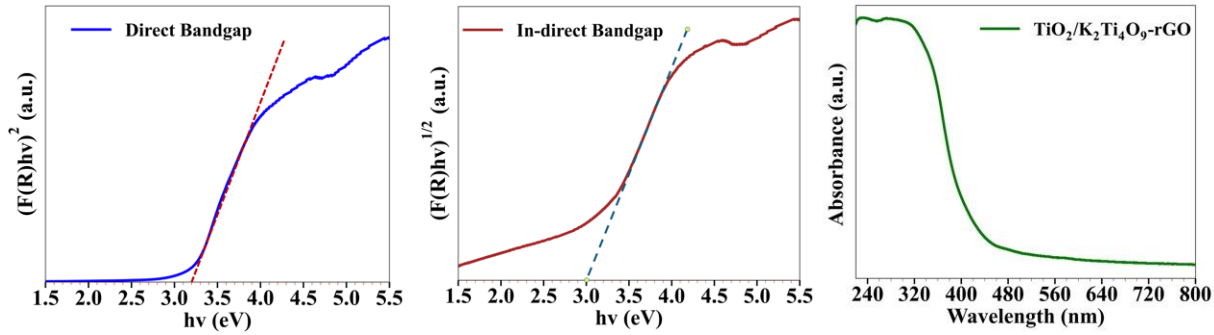

Figure S4*: Optical bandgap determination of $TiO_2/K_2Ti_4O_9$–rGO nanocomposites.* *Kubelka–Munk transformed UV–Vis diffuse reflectance spectra used to estimate (a) direct and (b) indirect bandgaps. The broadened absorption reflects synergistic electronic interactions between TiO_2 polymorphs, $K_2Ti_4O_9$, and rGO.*

5. Electronic Structure from UPS

Ultraviolet photoelectron spectroscopy (UPS) was used to determine the work function and valence-band positions of the $TiO_2/K_2Ti_4O_9$–rGO nanocomposite (**Figure S5**). Combined with the optical-gap estimates, these data were used to construct the schematic band-alignment diagram shown in **Figure S6**. The work function (Φ) was calculated using:

$$\Phi = h\nu - E_{cutoff} \quad (5)$$

where $h\nu$ is the photon energy of the UV source and E_{cutoff} is the secondary electron cut-off energy. The derived band positions indicate favourable alignment for photo-assisted charge separation. Individually, $K_2Ti_4O_9$ exhibits valence and conduction band positions of +3.06 V and −0.48 V versus NHE (pH 7), respectively, while anatase TiO_2 and TiO_2 (B) show VB/CB values of +2.67/−0.53 V and +2.34/−0.56 V. In the composite, the effective band edges are located at approximately +0.6 V (VB) and −2.4 V (CB) versus NHE (pH 7), enabling efficient utilisation of photogenerated charge carriers (**Figure S6**).

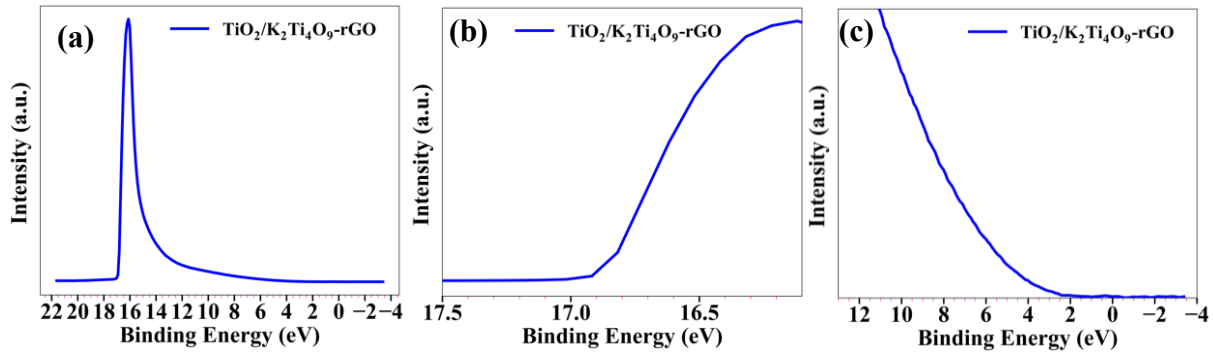

Figure S5: ***Ultraviolet photoelectron spectroscopy (UPS) analysis of $TiO_2/K_2Ti_4O_9$–rGO.*** ***(a)*** *Full UPS spectrum,* ***(b)*** *secondary electron cut-off region used to determine the work-function, and* ***(c)*** *magnified Fermi-level region. These data were used to derive the band alignment and energy level diagram.*

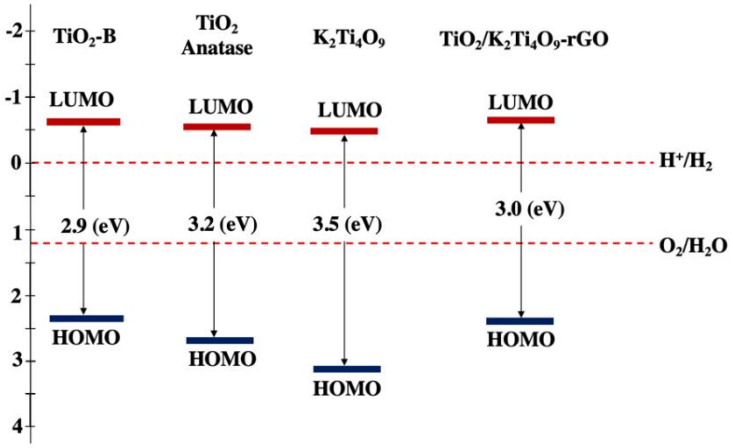

Figure S6: ***Energy band structure of the TiO_2, $K_2Ti_4O_9$, and $K_2Ti_4O_9$-rGO nanocomposite.*** *Schematic illustration of conduction band, valence band, and Fermi-level positions derived from UPS and optical bandgap measurements, highlighting favourable band alignment for photo-assisted charge separation.*

6. Electrode Morphology and Architecture

Scanning electron microscopy (SEM) reveals the structural evolution from multiphase powder to a hierarchically integrated carbon-felt-supported electrode (**Figure S7)**. The TiO2/$K_2Ti_4O_9$–rGO active material forms a uniform and conformal coating throughout the three-dimensional carbon felt network without blocking macropores. This architecture enables continuous electronic pathways through rGO and carbon fibres while maintaining short Li^+ diffusion distances within the oxide phases. Energy-dispersive X-ray spectroscopy (EDS) mapping confirms homogeneous spatial distribution of Ti, K, O, and C across the electrode.

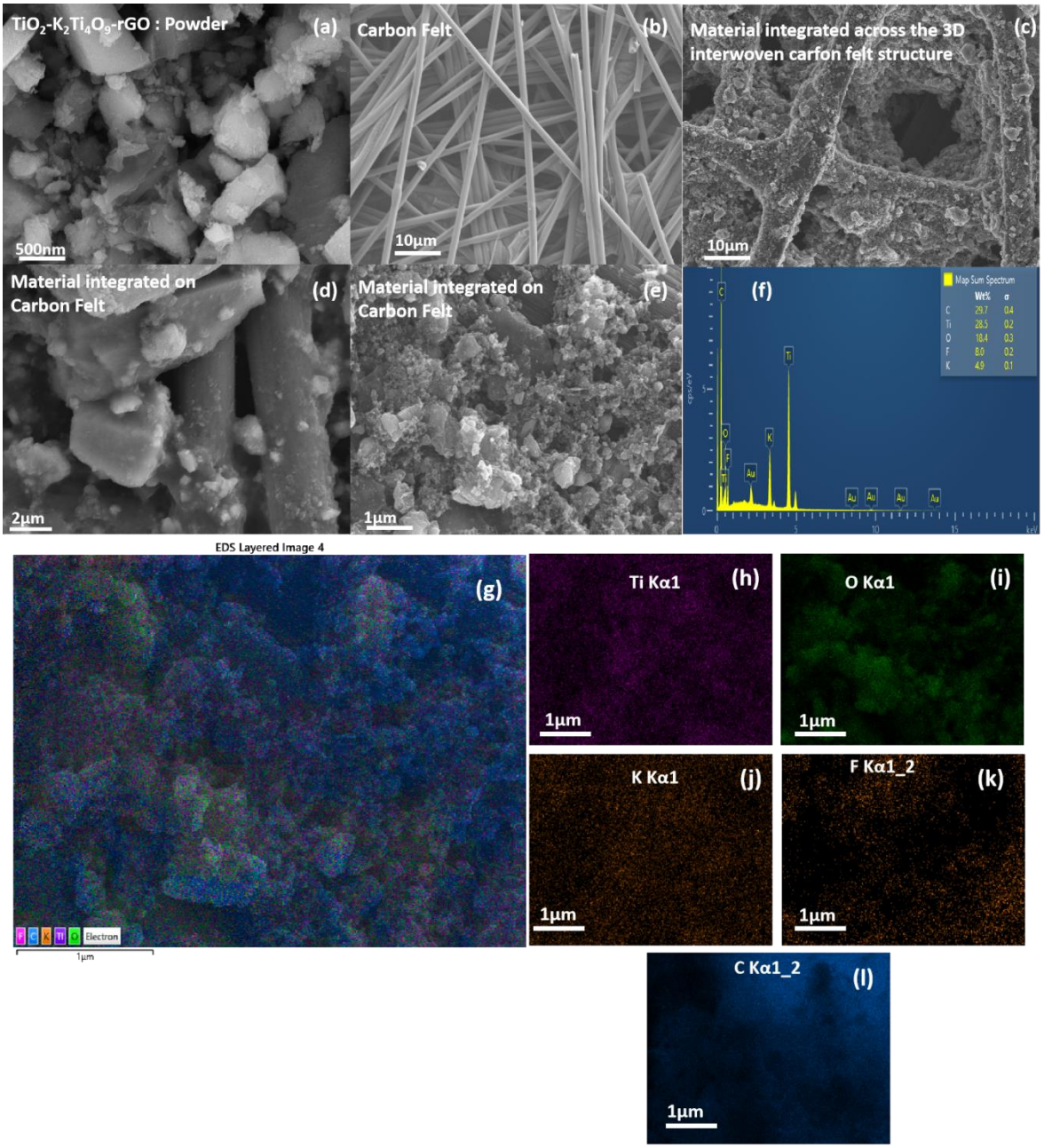

Figure S7. ***Morphological and compositional uniformity of the TiO₂/K₂Ti₄O₉–rGO carbon-felt electrode (fresh).*** ***(a)*** *SEM image of* ***TiO₂/K₂Ti₄O₉–rGO*** *powder,* ***(b)*** *pristine carbon felt, and* ***(c–e)*** *electrode after slurry deposition showing uniform coating and strong integration within the 3D carbon-felt network.* ***(f)*** *EDS spectrum and* ***(g–l)*** *elemental maps confirm homogeneous spatial distribution of Ti, K, O, and C, supporting uniform electrochemical accessibility across the electrode.*

7. Electrochemical Performance: Phase and Light Effects

Comparative electrochemical measurements demonstrate that the $TiO_2/K_2Ti_4O_9$–rGO electrode significantly outperforms pure TiO_2 and $TiO_2/K_2Ti_4O_9$ electrodes under both dark and illuminated conditions (**Figures 2 and S8**). Under illumination, cyclic voltammetry and galvanostatic charge–discharge measurements reveal enhanced redox activity, reduced polarisation, and improved capacity retention over 300 cycles, highlighting the synergistic effect of multiphase architecture and photo-assisted processes.

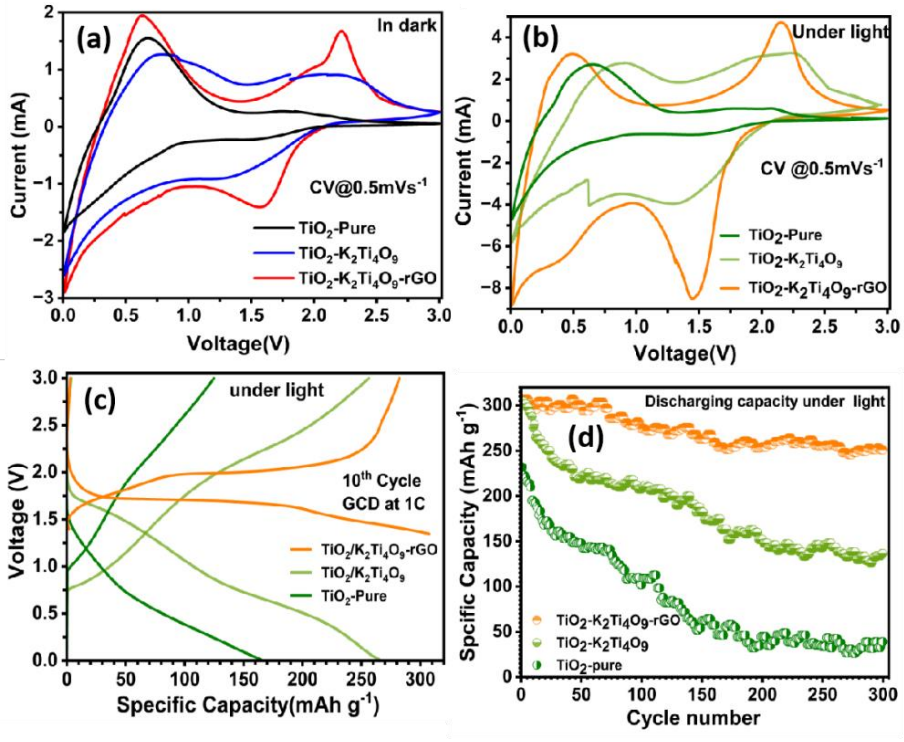

Figure S8: Electrochemical performance comparison of different electrodes. ***(a)*** *Cyclic voltammetry at 0.5 mV s^{-1} in the dark.* ***(b)*** *Cyclic voltammetry under illumination,* ***(c)*** *galvanostatic charge-discharge profiles at 1C, and* ***(d)*** *cycling stability over 300 cycles under illumination for pure TiO_2, TiO_2/ $K_2Ti_4O_9$, and $TiO_2/K_2Ti_4O_9$-rGO electrodes.*

8. Electrochemical performance of $TiO_2/K_2Ti_4O_9$-rGO electrodes in dark and light conditions

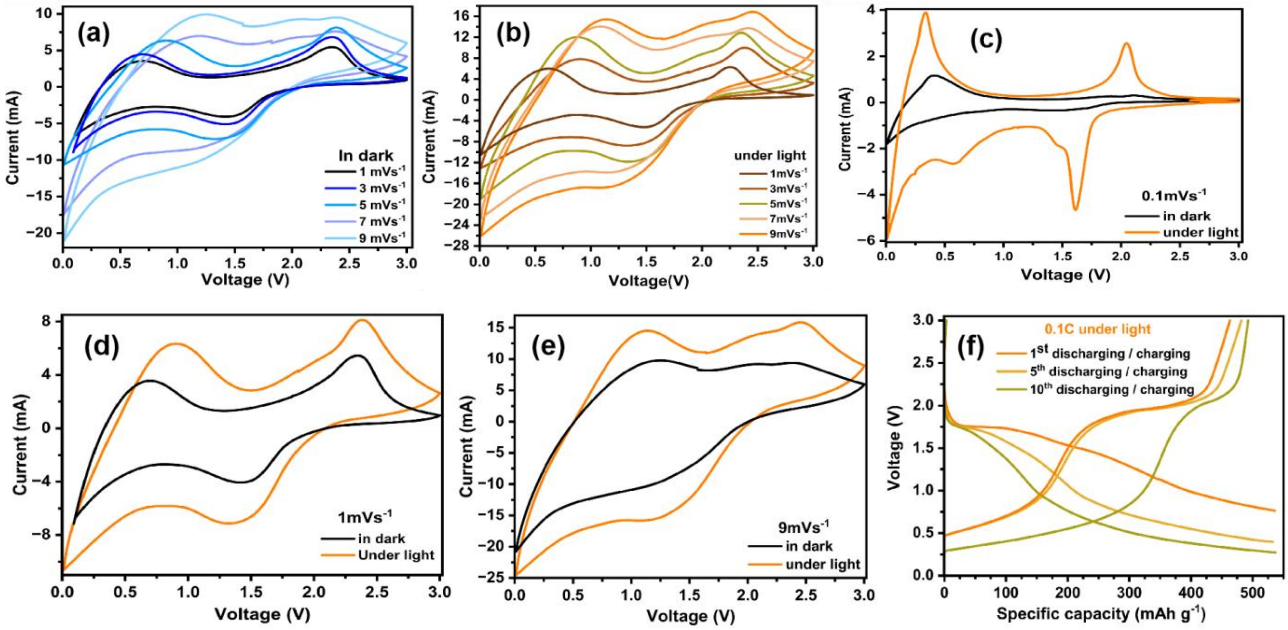

Figure S9. Electrochemical response of *$TiO_2/K_2Ti_4O_9$–rGO* under dark and light conditions. ***(a)*** *CV curves at scan rates from 1 to 9 mV s^{-1} in the dark,* ***(b)*** *CV curves under illumination showing enhanced current response,* ***(c-e)*** *comparison of CV curves at low and high scan rates highlighting increased charge-storage area under light, and* ***(f)*** *galvanostatic charge–discharge profiles at 0.1C under illumination, showing the 1st, 5th, and 10th cycles.*

9. Charge-Storage Mechanism Analysis

The relative contributions of surface-controlled (pseudocapacitive) and diffusion-controlled Li^+ storage were quantified using Trasatti's method:[3,4]

$$I = k_1 v + k_2 v^{1/2} \quad (6)$$

Analysis of scan-rate-dependent CV data shows that illumination consistently enhances diffusion-controlled Li^+ contribution across all scan rates (**Figs. S10c and d**), indicating accelerated Li^+ transport and improved charge-transfer kinetics under photo-assisted operation.

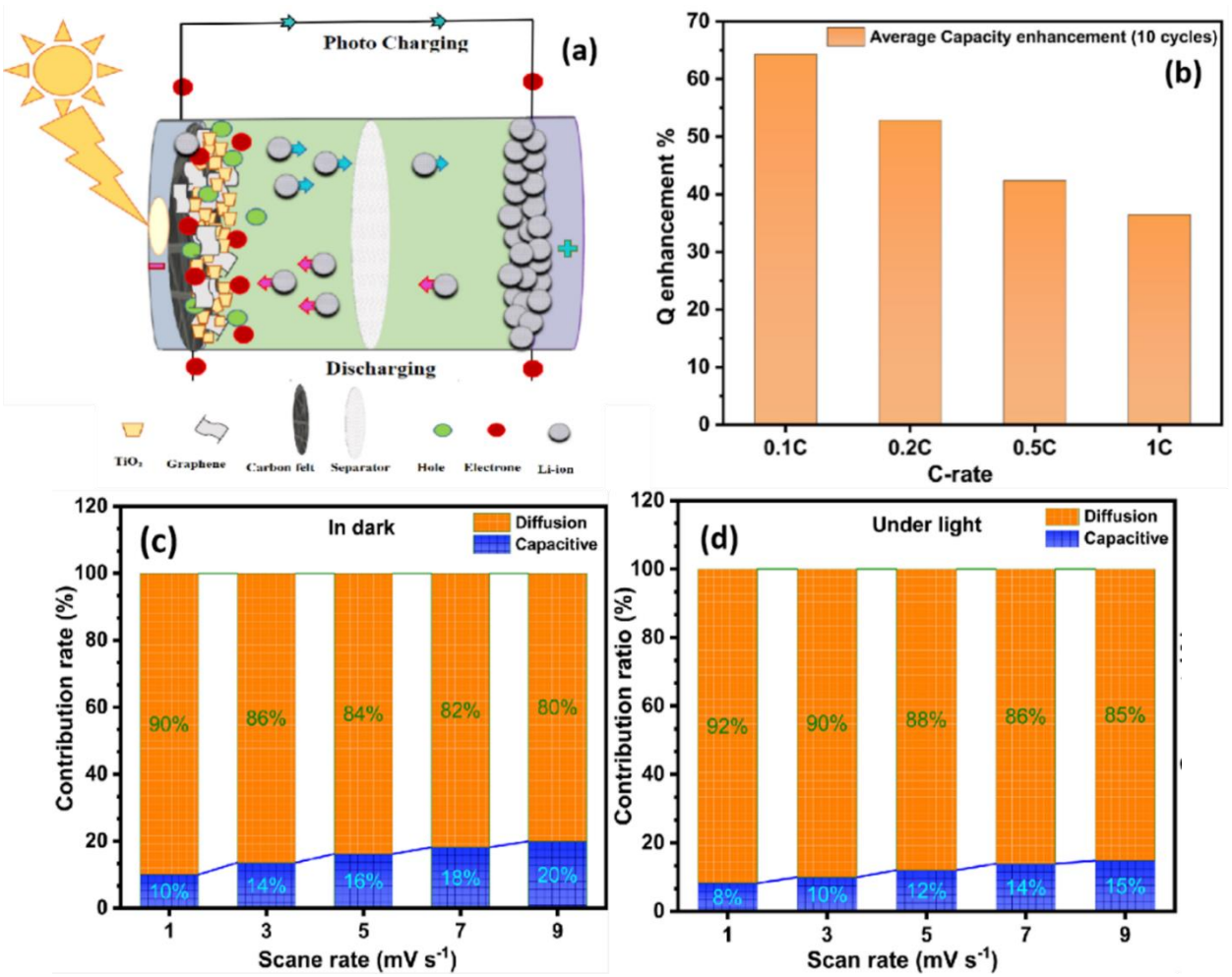

Figure S10: Photo-assisted lithium storage kinetics and mechanism. ***(a)*** *Schematic illustration of photo-assisted lithiation/delithiation in the carbon-felt-supported $TiO_2/K_2Ti_4O_9$–rGO electrode,* ***(b)*** *average capacity enhancement under illumination at different scan rates, and* ***(c,d)*** *relative contributions of surface-controlled (capacitive) and diffusion-controlled processes at different scan rates.*

10. Photo-Assisted Lithium Storage Mechanism

The photo-assisted lithiation–delithiation mechanism is schematically illustrated in Figure **S10a**. Upon illumination, photogenerated electrons in TiO_2 polymorphs and layered $K_2Ti_4O_9$ are rapidly extracted through the rGO network and carbon felt to the external circuit, facilitating Li^+ reduction at the counter electrode. Simultaneously, photogenerated holes promote Li^+ deintercalation from the oxide lattice. This dual functionality enables concurrent light harvesting and electrochemical energy storage.

Table S2. ***Lithium-ion diffusion coefficients (DLi⁺) for $TiO_2/K_2Ti_4O_9$–rGO under dark and illuminated conditions.*** *Diffusion coefficients were extracted from Randles–Ševčík analysis of CV peak currents.*

Redox Peaks in dark	Diffusion coefficient, D_{Li+} ($cm^2\ s^{-1}$)	Redox Peaks under light	Diffusion coefficient, D_{Li+} ($cm^2\ s^{-1}$)
P1 at 0.62 V	7.9×10^{-10}	P1at 0.69 V	3.7×10^{-8}
P2 at 2 V	3.6×10^{-10}	P2 at 2.1V	4.1×10^{-8}
P3 at 1.68 V	2.8×10^{-10}	P3 at1.5 V	1.6×10^{-8}

11. Electrode Recovery and Fatigue Resistance

Capacity recovery experiments demonstrate that illumination enables effective regeneration of fatigued electrodes (**Figure S11d and e**). Under prolonged dark cycling at 1C, capacity decreases from ~225 to ~74 mAh g^{-1} with a concomitant reduction in open-circuit voltage (OCV) from ~3.0 to ~0.5 V, indicating increased polarisation and suppressed redox activity. A 3 h dark rest results in only partial recovery. In contrast, illumination of the fatigued electrode for 3 h restores the capacity to ~154 mAh g^{-1} (~68% of the initial value) and increases the OCV to ~1.67 V, followed by stabilised cycling performance. This behaviour highlights the role of photogenerated carriers in relieving strain, reopening Li^+ diffusion pathways, and reactivating Ti^{4+}/Ti^{3+} redox processes (**Figure 5**).

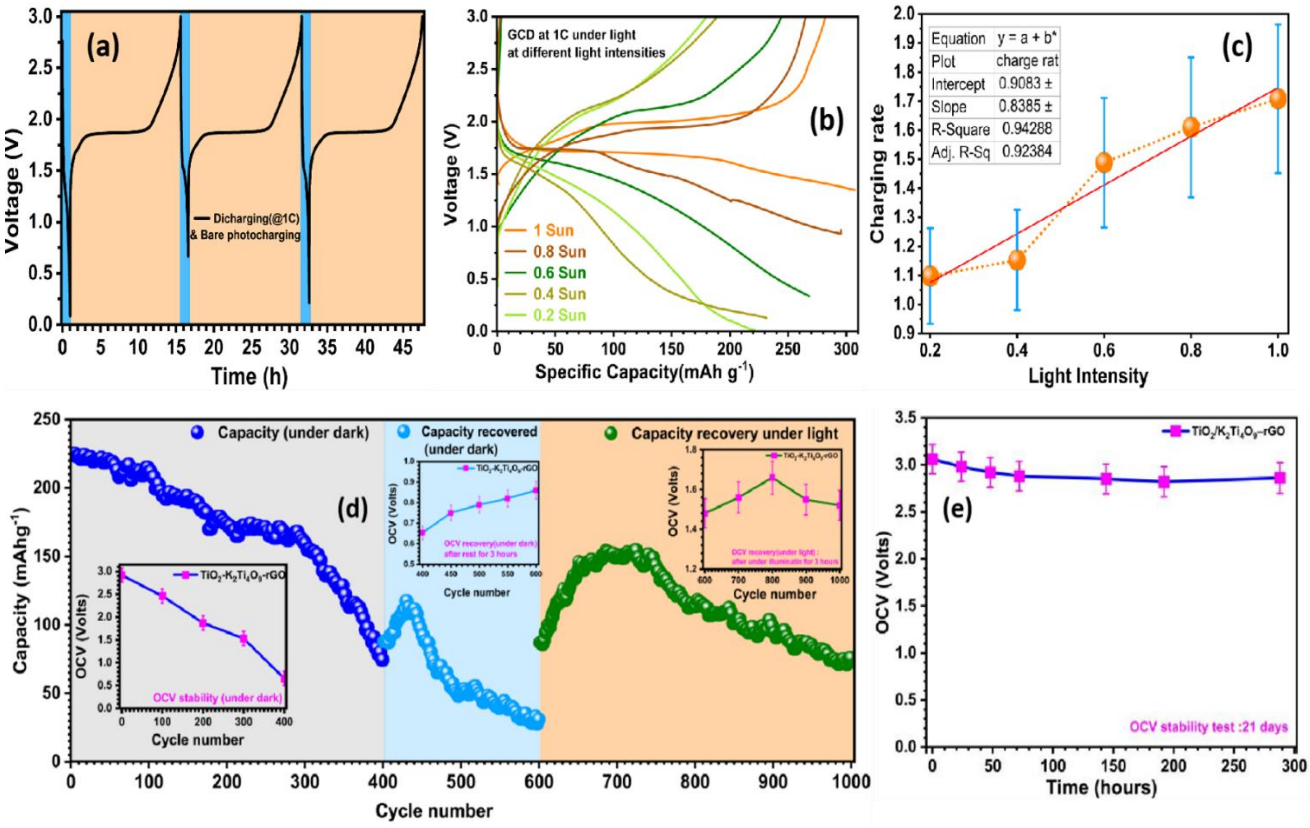

Figure S11: Photo-assisted charging behaviour and electrode recovery. ***(a)*** *Bare light-charging (without current) and dark-discharging cycles at 1C,* ***(b,c)*** *photo-assisted charging under different light intensities (0.2–1 sun) and corresponding charging-rate dependence, and* ***(d,e)*** *battery recovery test demonstrating light-induced restoration of capacity in a fatigued electrode. Light restores the capacity of a severely fatigued electrode (13% capacity, <30 mAh g^{-1}) to ~153 mAh g^{-1} (~70% of its initial value), consistent with photocarrier-assisted strain relaxation and reactivation of reversible redox processes.*

12. Light-to-Electrochemical Conversion Efficiency

The light-to-electrochemical conversion efficiency (η) was calculated from optical input energy and achieved electrochemical output energy. The calculated η ≈ 0.18% confirms direct conversion of photonic energy into stored electrochemical energy.

Calculation for light-to-electrochemical conversion efficiency (η):

1. Optical Input Energy

$$P_{in} = I_{light} \times A.$$

$$P_{in} = 0.100\ W \cdot cm^{-2} \times 2.010\ cm^2 = 0.2010\ W$$

$$E_{input,\ light} = P_{in} \times t_{photo}$$

$$E_{input,light}t = 0.2010\ W \times 15.0\ h = 3.015\ Wh$$

$$E_{input,light} = 3.015\ Wh \times 3600\ s \cdot h^{-1} = 10{,}854\ J$$

2. Output Electrochemical Energy

$$E_{output}t = \int (V_{dark,CC} - x)\ dC$$

For constant-current discharge:

$$E_{output} \approx I \int (V(t) - x)\ dt$$

If $(V(t) - x) \approx (V_{avg} - x)$:

$$E_{output} \approx I\ (V_{avg} - x)\ t_{dis}$$

For x ≈ 0:

$$E_{output} = I \times V_{avg} \times t_{dis}$$

$$E_{output} = 0.002240\ A \times 2.40\ V \times 1.0\ h = 0.005376\ Wh$$

$$E_{output} = 0.005376\ Wh \times 3600\ s \cdot h^{-1} = 19.35\ J$$

3. Light-to-Electrochemical Conversion Efficiency

$$\eta = E_{output} / E_{input,light}$$

$$\eta = 0.005376\ Wh / 3.015\ Wh = 1.783 \times 10^{-3}$$

$$\eta \approx 0.178\ \%$$

13. Post-Mortem Analysis and SEI Evolution

Post-cycling SEM, EDS, Raman spectroscopy, XPS, and electrochemical impedance spectroscopy (EIS) reveal that long-term performance decay is governed primarily by progressive formation of a $LiPF_6$-derived solid electrolyte interface (SEI) (**Figures S12**). While EDS confirms a homogeneous and preserved Ti, K, and O distribution, demonstrating structural integrity of the $TiO_2/K_2Ti_4O_9$ framework, the emergence of F and P signals evidence electrolyte decomposition and accumulation of SEI species (e.g., LiF, Li_2CO_3, $Li_xPO_\gamma Fz$). Raman spectra of discharged electrodes show broad features in the 400–900 cm^{-1} region characteristic of SEI components (**Figure S12b**).

Concurrent attenuation of Ti–O vibrational modes and SEM observations confirm progressive masking of photoactive surfaces. This leads to increased charge-transfer resistance, as reflected by EIS: compared with the fresh electrode (R_{ct} ≈ 50 Ω in the dark and ≈ 33 Ω under illumination),

R_{ct} increases significantly after 300 (≈ 165 Ω in the dark and ≈ 140 Ω under illumination), accounting for the gradual capacity decay during long-term cycling.

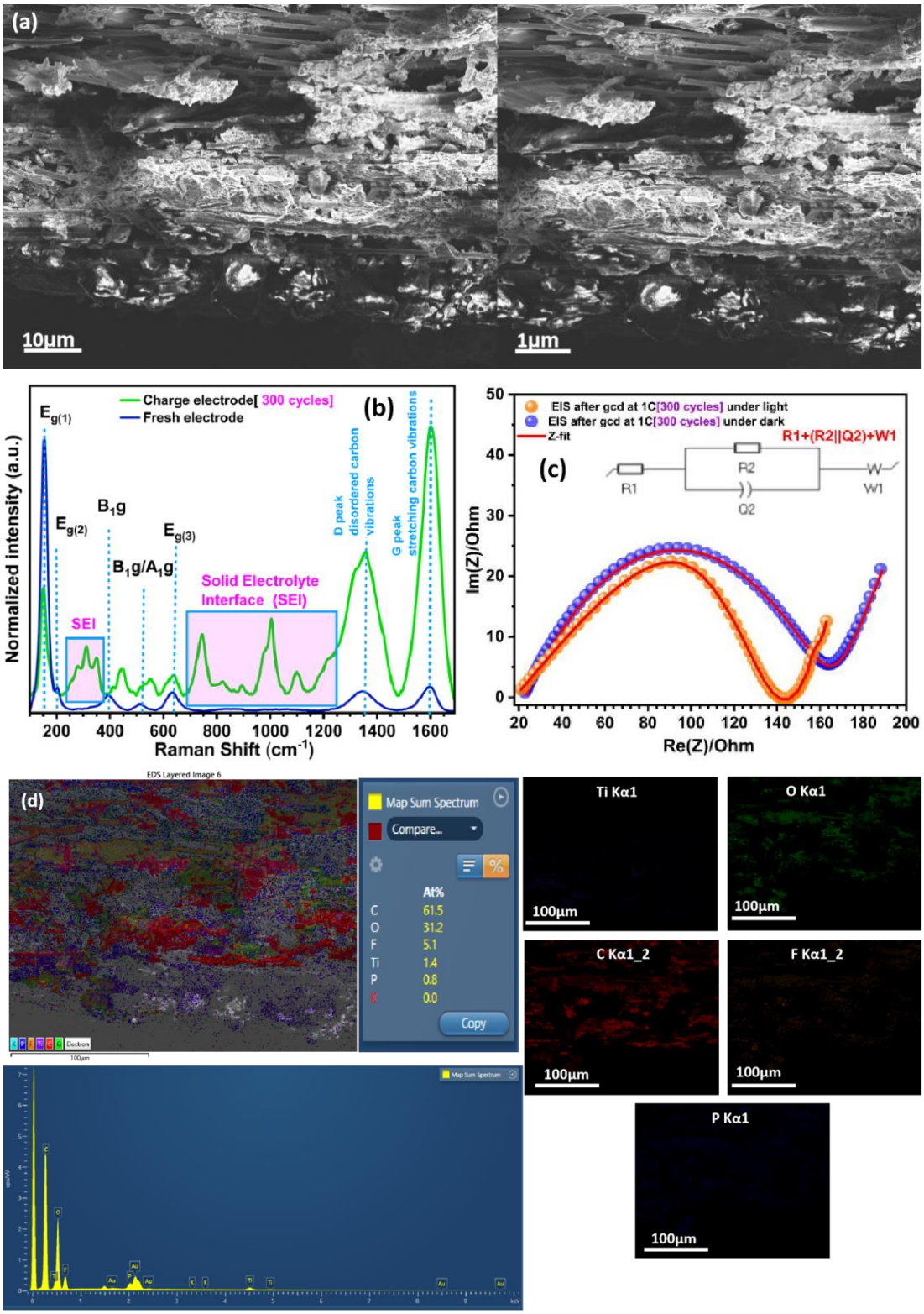

Figure S12: ***Post-mortem analysis of SEI-dominated degradation after 300 charge–discharge cycles. (a)*** *SEM image of the cycled electrode,* ***(b)*** *Raman spectra of fresh (blue)and light-discharged (green) electrodes,* ***(c)*** *electrochemical impedance spectra measured in the dark and under illumination, revealing increased interfacial resistance after prolonged cycling.****(d)*** *EDS spectrum and elemental maps confirming widespread F and P distribution arising from $LiPF_6$-derived SEI formation.*

14. XPS of cycled electrodes

Analysis of O 1s, C 1s, F 1s, and P 2p spectra reveals the formation of $LiPF_6$-derived SEI species under both dark and illuminated conditions (**Figs. S13–S14**). However, electrodes cycled under illumination show suppressed high-binding-energy phosphate and fluorophosphate components, indicating delayed growth of mechanically unstable, resistive interphases. This demonstrates that both light and strain-stabilised lattices significantly delay fatigue-driven interfacial thickening.

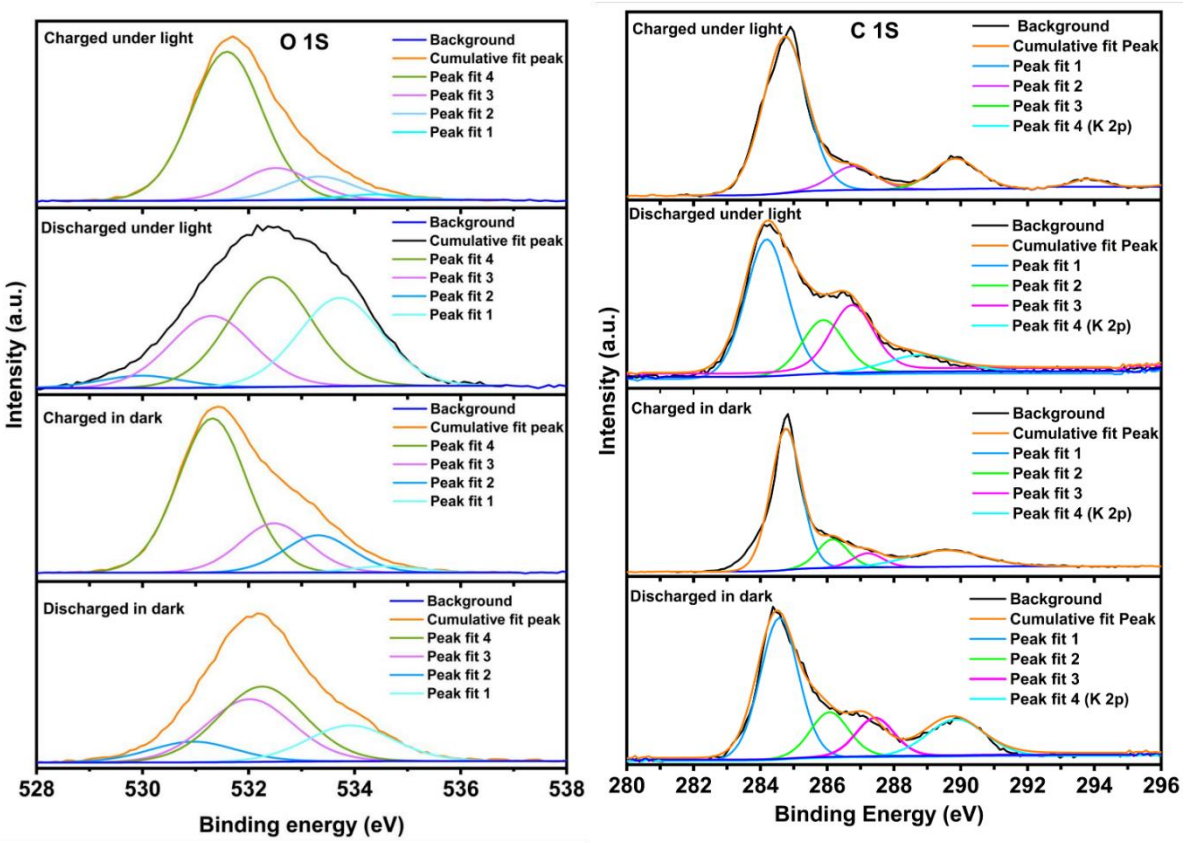

Figure S13: *O 1s and C 1s XPS spectra of cycled electrodes at various charge/discharge states. K 2p peaks overlap with C 1s peaks*

Table S3: ***Reference Raman peak assignments for SEI components in $LiPF_6$/EC–DEC electrolyte systems.*** *Peak positions correspond to commonly reported vibrational modes of inorganic and organic SEI species and may overlap with TiO_2 or rGO features.*

SEI Compound	Raman Shift (cm^{-1})	Notes
Li_2CO_3	~1085	Strong sharp peak; key inorganic SEI component
LiF	~320–330	Weak Raman signal; often missed without enhancement
Li_2O	~520–540	Can overlap with TiO_2 or Si peaks
$ROCO_2Li$ / ROLi	~1300–1600	Broad bands; overlaps with rGO D/G bands
LiOH	~365–370	Weak; observed in extended charge/discharge cycles
Residual $LiPF_6$	~740–750, ~850–870	Can be seen in thick solid electrolyte inter-phase (SEI) regions
EC/DEC Residues	~880, ~1085–1120	Carbonate-related; overlap with Li_2CO_3
rGO D-band	~1350	Disorder-induced; overlaps with $ROCO_2Li$
rGO G-band	~1580	Graphitic vibration; overlaps with organics

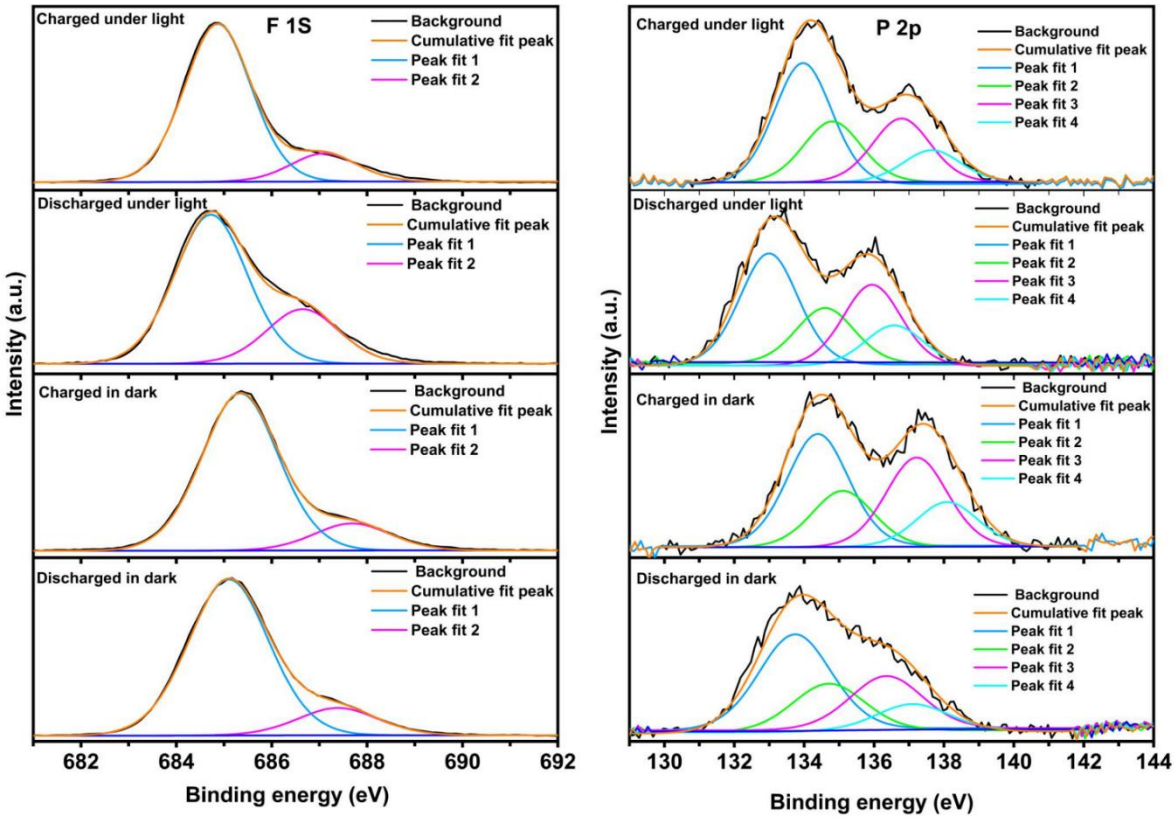

Figure S14: *F 1s and P 2p XPS spectra of cycled electrodes at various charge/discharge states*

15. Interfacial SEI Evolution Revealed by In-Situ Raman Spectroscopy and Its Impact on Electrochemical Performance

In-situ Raman spectroscopy provides direct insight into the evolution of interfacial chemistry and its correlation with electrochemical degradation in the TiO_2–$K_2Ti_4O_9$–rGO electrode. During the early cycling stage (10–50 cycles), the Raman spectra are dominated by sharp Ti–O vibrational modes (E_g, B_{1g}, and A_{1g}), indicating preservation of the crystalline titanate framework. Concurrently, the rGO D and G bands remain well defined, reflecting a continuous and conductive carbon network. In this regime, galvanostatic charge–discharge profiles exhibit clear voltage plateaux and high reversible capacities (~225 mAh g^{-1}), consistent with efficient Li^+ intercalation and rapid charge transport. With continued cycling (≈100–200 cycles), additional Raman features associated with $LiPF_6$ decomposition and carbonate-rich solid electrolyte interface (SEI) species progressively emerge.

At extended cycling (200–300 cycles), SEI-related Raman bands dominate the spectra, while Ti–O vibrational signatures are strongly suppressed. Collectively, the in-situ Raman results demonstrate that uncontrolled SEI growth progressively blocks Ti–O active sites and disrupts electronic pathways, ultimately governing long-term performance decay.

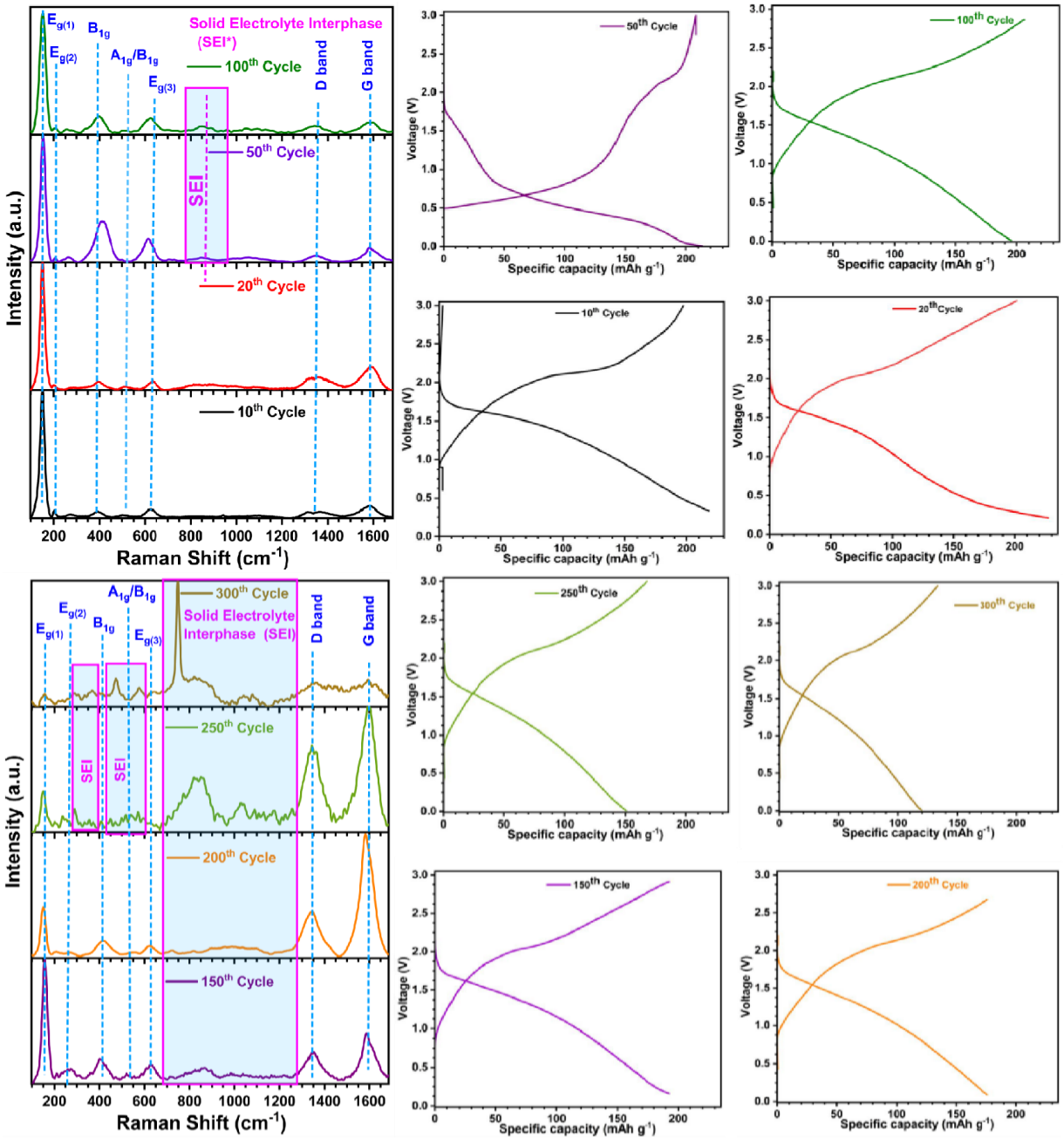

Figure S15. ***In-situ Raman spectroscopy of SEI evolution during cycling.*** *Progressive emergence of $LiPF_6$-derived SEI signatures and attenuation of Ti–O vibrational modes with cycling, revealing interfacial masking of active sites and disruption of charge-transport pathways.*

16. Fresh Electrode Analysis by Confocal Raman Imaging and NNLS

Confocal Raman mapping was employed to establish the spatial and chemical distribution of phases within the fresh $TiO_2/K_2Ti_4O_9$–rGO electrode supported on carbon felt prior to electrochemical cycling. Due to substantial spectral overlap between TiO_2 polymorphs and $K_2Ti_4O_9$, non-negative least squares (NNLS) unmixing was applied to quantitatively separate the contributions of anatase TiO_2, TiO_2(B), $K_2Ti_4O_9$, and rGO.

The reference spectra include characteristic Raman-active modes of the TiO_2 polymorphs alongside the D (~1350 cm^{-1}) and G (~1580 cm^{-1}) bands of rGO, enabling reliable component discrimination. Raman mapping was focused on the deposited active layer; the carbon felt

substrate lies beneath the focal plane and contributes minimally to the collected spectra. Moreover, the broader band shapes and higher disorder-related intensity ratios of rGO enable its clear distinction from the more graphitic carbon felt within the NNLS framework.

The resulting NNLS fraction maps reveal a chemically heterogeneous yet well-integrated electrode architecture. Anatase TiO_2, which constitutes the largest phase fraction (37.4%), is uniformly distributed across the mapped region, forming a continuous photoactive matrix. TiO_2 (B) (18.8%) and $K_2Ti_4O_9$ (29.8%) exhibit more localised and clustered distributions, reflecting their distinct crystallographic and morphological characteristics. The rGO component (13.9%) forms a nanoscale, percolating conductive network that bridges oxide domains, promoting efficient local electron transport and suppressing charge recombination. The carbon felt functions as a macroscopic current collector, providing mechanical support and long-range electronic conductivity. Compared with simple Raman intensity mapping, NNLS unmixing provides a more quantitative representation of the multiphase system and establishes a robust baseline for analysing cycling-induced interfacial evolution.

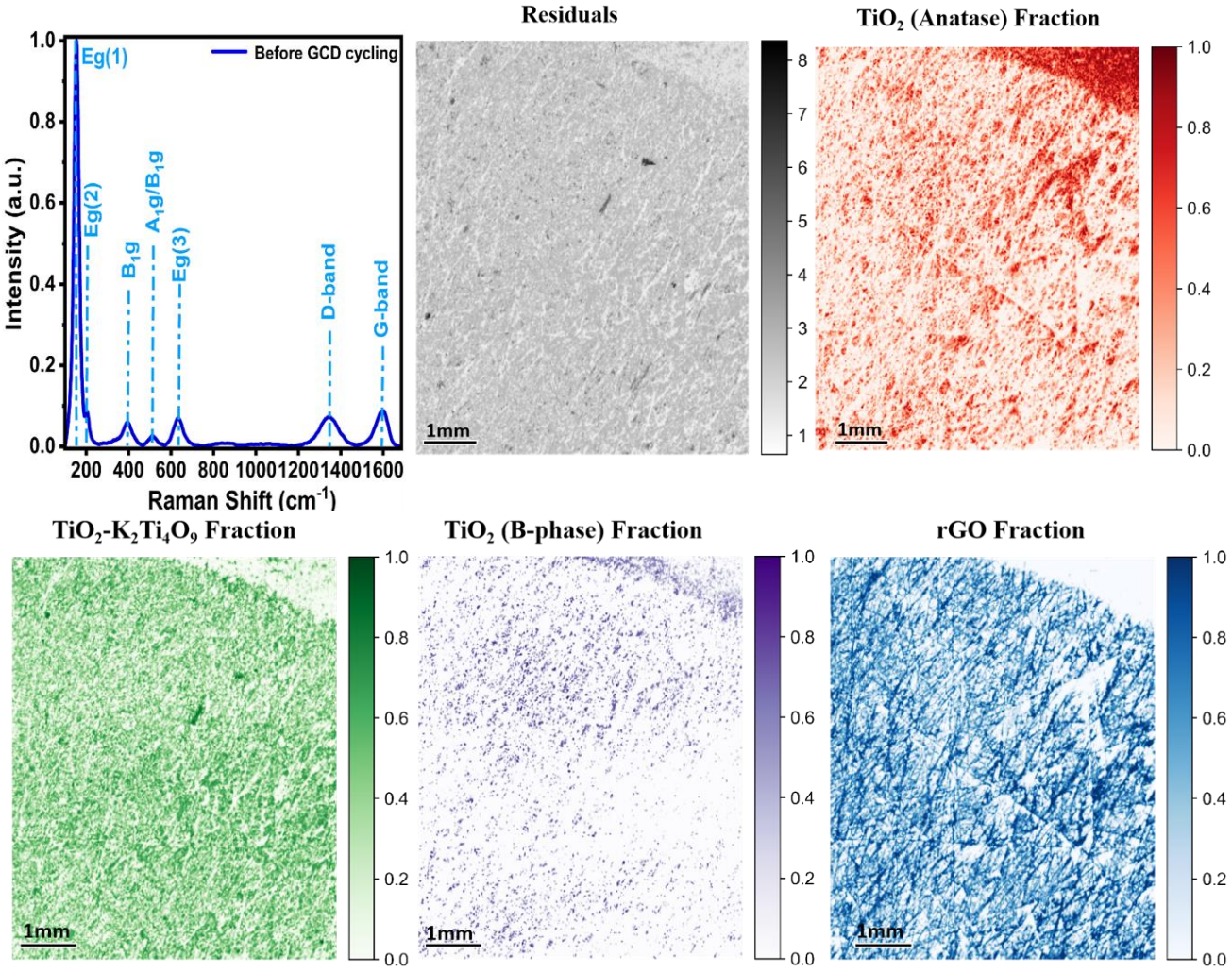

Figure S16. ***Confocal Raman mapping of the fresh TiO_2/$K_2Ti_4O_9$–rGO electrode.*** *Normalised Raman maps and NNLS-derived fraction maps showing the spatial distribution of anatase TiO_2, TiO_2(B), $K_2Ti_4O_9$, and rGO within the active layer on carbon felt. Reference spectra of all components are included.*

17. Rate Capacity Comparison across 300 GCD Cycles (Dark and Light Conditions)

The relationship between rate capability and specific capacity further highlights the performance advantage of the TiO_2–$K_2Ti_4O_9$–rGO electrode relative to previously reported TiO_2-based systems.[5-15] Most literature electrodes cluster within a moderate capacity range (~80–250 mAh g^{-1}) and exhibit limited rate capability, particularly under dark conditions, where achievable rate capacities typically remain below ~120 mAh g^{-1}.

In contrast, the present electrode delivers both higher specific capacity and superior rate performance. Under dark operation, it maintains a rate capacity of ~138 mAh g^{-1} at a substantially higher specific capacity (~325 mAh g^{-1}). Under illumination, the electrode shifts into a high-performance regime, achieving a specific capacity of ~534 mAh g^{-1} together with enhanced rate capability (~180–200 mAh g^{-1}). This simultaneous enhancement of capacity and rate performance under light is rarely reported for titanate-based electrodes and reflects the synergistic effects of multiphase strain engineering, optimised band alignment, and efficient photo-assisted charge transport through the rGO network.

Table S4. ***Comparison of rate capability and specific capacity of TiO_2-based electrodes reported in the literature and this work.*** *Data are compared at similar current densities or C-rates; illumination conditions are explicitly indicated where applicable.*

No	Sample	Type	Specific capacity	Rate	Light	References
1	TiO_2	anatase /rutile	180 mAh g^{-1} (0.2 A g^{-1})	180 mAh g^{-1} ~140 mAh g^{-1} (0.2~3 A g^{-1})	/	5
2	TiO_2	anatase	110 mAh g^{-1} (0.2 A g^{-1})	110 mAh g^{-1} ~45 mAh g^{-1} (0.2~2 A g^{-1})	/	6
3	TiO_2	anatase	130 mAh g^{-1} (0.15 A g^{-1})	130 mAh g^{-1} ~85 mAh g^{-1} (0.15~0.6 A g^{-1})	/	7
4	TiO_2	anatase	150 mAh g^{-1} (0.5 A g^{-1})	130 mAh g^{-1} ~115 mAh g^{-1} (0.5~1.5 A g^{-1})	/	8
5	TiO_2	anatase	90 mAh g^{-1} (0.15 A g^{-1})	90 mAh g^{-1} ~25 mAh g^{-1} (0.15~3 A g^{-1})	/	9
6	TiO_2	anatase	210 mAh g^{-1} (0.2 A g^{-1})	210 mAh g^{-1} ~160 mAh g^{-1} (0.2~2 A g^{-1})	/	10

7	TiO_2	anatase	160 mAh g^{-1} (0.1 A g^{-1})	160 mAh g^{-1} ~50 mAh g^{-1} (0.1~3 A g^{-1})	/	11
8	Ag/TiO_2	anatase	150 mAh g^{-1} (0.1 A g^{-1})	150 mAh g^{-1} ~55 mAh g^{-1} (0.1~1 A g^{-1})	/	12
9	TiO_2	anatase	140 mAh g^{-1} (0.15 A g^{-1})	140 mAh g^{-1} ~55 mAh g^{-1} (0.15~1.5 A g^{-1})	/	13
10	TiO_2	anatase	85 mAh g^{-1} (0.2 A g^{-1})	185mAhg^{-1} ~88 mAh g^{-1} (0.2A g^{-1}~3Ag^{-1})	218 mAh g^{-1} ~121mAh g-^{1} (0.2Ag-^{1} ~3 A g-^{1})	14
11	Au-TiO_2	anatase	205 mAh g^{-1} (0.2 A g^{-1})	205 mAh g^{-1} ~105 mAh g^{-1} (0.2Ag^{-1}~3 A g^{-1})	276 mAh g^{-1} ~163 mAh g^{-1} (0.2 A g^{-1} ~3 A g^{-1})	15
12	TiO_2-$K_2Ti_4O_9$-rGO	multiphase strain-engineered	325 mAh g^{-1} (0.1C)-in dark 534 mAh g^{-1} (0.1C) under light	325 mAhg^{-1} ~138 mAh g^{-1} (0.1 C~2C)	534 mAh g^{-1} ~185 mAh g^{-1} (0.1 C~2C)	This work

References

1 G. Gouadec and P. Colomban, *Prog. Cryst. Growth Charact. Mater.,*, 2007, **53**, 1–56.

2 T. M. G. Mohiuddin, A. Lombardo, R. R. Nair, A. Bonetti, G. Savini, R. Jalil, N. Bonini, D. M. Basko, C. Galiotis, N. Marzari, K. S. Novoselov, A. K. Geim and A. C. Ferrari, *Phys. Rev. B*, 2009, **79**, 205433.

3 R. Khatoon, M. Nazir, R. T. Baker, M. Billing, S. Babar, S. Kellici, S. Dunn and M. T. Sajjad, *Adv. Funct. Mater.*, 2025, **35**, 2501498.

4 T. Brezesinski, J. Wang, S. H. Tolbert and B. Dunn, *Nat. Mater.*, DOI:10.1038/NMAT2612.

5 W. Song, Q. Jiang, X. Xie, A. Brookfield, E. J. L. McInnes, P. R. Shearing, D. J. L. Brett, F. Xie and D. J. Riley, *Energy Storage Mater.*, 2019, **22**, 441–449.

6 M. Gao, Y. Bao, Y. Qian, Y. Deng, Y. Li and G. Chen, *Inorg. Chem.*, 2018, **57**, 12245–12254.

7 J. Ma, K. G. Reeves, A. G. Porras Gutierrez, M. Body, C. Legein, K. Kakinuma, O. J. Borkiewicz, K. W. Chapman, H. Groult, M. Salanne and D. Dambournet, *Chemistry of Materials*, 2017, **29**, 8313–8324.

8 Y. Cai, H. E. Wang, X. Zhao, F. Huang, C. Wang, Z. Deng, Y. Li, G. Cao and B. L. Su, *ACS Appl. Mater. Interfaces*, 2017, **9**, 10652–10663.

9 M. Zhang, K. Yin, Z. D. Hood, Z. Bi, C. A. Bridges, S. Dai, Y. S. Meng, M. P. Paranthaman and M. Chi, *J. Mater. Chem. A Mater.*, 2017, **5**, 20651–20657.

10 D. H. Lee, B. H. Lee, A. K. Sinha, J. H. Park, M. S. Kim, J. Park, H. Shin, K. S. Lee, Y. E. Sung and T. Hyeon, *J. Am. Chem. Soc.*, 2018, **140**, 16676–16684.

11 Y. Qiu, K. Yan, S. Yang, L. Jin, H. Deng and W. Li, *ACS Nano*, 2010, **4**, 6515–6526.

12 Y. Zhang, J. Li, W. Li and D. Kang, *Materials 2019, Vol. 12,* DOI:10.3390/ma12162630.

13 T. D. Deepa, S. Mohapatra, S. V. Nair, A. S. Nair and A. K. Rai, *Sustain. Energy Fuels*, 2017, **1**, 138–144.

14 D. Imazeki, C. C. Van Gils, K. Nishio, R. Shimizu and T. Hitosugi, *ACS Appl. Energy Mater.*, 2020, **3**, 8338–8343.

15 Z. Ma, S. Wang, Z. Ma, J. Li, L. Zhao, Z. Li, S. Wang, Y. Shuang, J. Wang, F. Wang, W. Xia, J. Jian, Y. He, J. Wang, P. Guo and H. Wang, *Nano-Micro Letters 2024 17:1*, 2024, **17**, 74-.